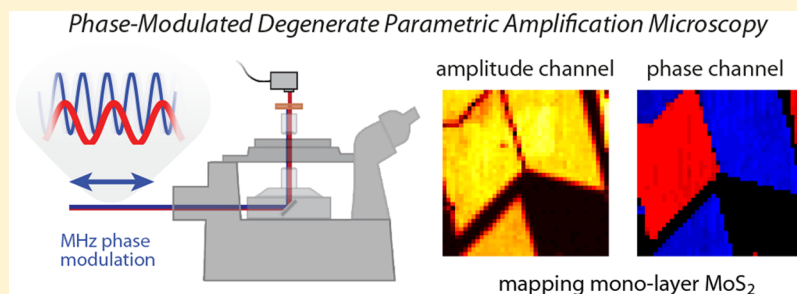


Phase-Modulated Degenerate Parametric Amplification Microscopy

Yunan Gao,^{†,||} Aaron J. Goodman,[‡] Pin-Chun Shen,[§] Jing Kong,^{§,†b} and William A. Tisdale^{*,†,†b}

[†]Department of Chemical Engineering, [‡]Department of Chemistry, and [§]Department of Electrical Engineering and Computer Sciences, Massachusetts Institute of Technology, Cambridge, Massachusetts 02139, United States

S Supporting Information



ABSTRACT: Second-order nonlinear optical interactions, including second-harmonic generation (SHG) and sum-frequency generation (SFG), can reveal a wealth of information about chemical, electronic, and vibrational dynamics at the nanoscale. Here, we demonstrate a powerful and flexible new approach, called phase-modulated degenerate parametric amplification (DPA). The technique, which allows for facile retrieval of both the amplitude and phase of the second-order nonlinear optical response, has many advantages over conventional or heterodyne-detected SHG, including the flexibility to detect the signal at either the second harmonic or fundamental field wavelength. We demonstrate the capabilities of this approach by imaging multigrain flakes of single-layer MoS₂. We identify the absolute crystal orientation of each MoS₂ domain and resolve grain boundaries with high signal contrast and sub-diffraction-limited spatial resolution. This robust all-optical method can be used to characterize structure and dynamics in organic and inorganic systems, including biological tissue, soft materials, and metal and semiconductor nanostructures, and is particularly well-suited for imaging in media that are absorptive or highly scattering to visible and ultraviolet light.

KEYWORDS: Second-harmonic generation, super-resolution, MoS₂, grain boundary, 2D, transition metal dichalcogenide

Second-harmonic generation (SHG) and sum-frequency generation (SFG) microscopy are powerful tools for characterizing structure and dynamics in low-dimensional materials, biological tissues, and at interfaces between centrosymmetric media.^{1–6} However, conventional SHG imaging reveals only the squared magnitude of the second-harmonic field—not its phase.^{1–5} To overcome this limitation, phase-sensitive variants of SHG and SFG microscopy, based on the principle of heterodyne detection, have been developed;^{7–13} examples include interferometric SHG (I-SHG) microscopy^{7–10} and second-harmonic digital holographic microscopy.^{10,13}

In heterodyne SHG, a second-harmonic signal field is generated within the sample and then mixed with a reference field to retrieve its amplitude and phase. In our previous work,¹⁴ we showed that when an optical field and its second harmonic are temporally coincident within the sample—as is sometimes the case in I-SHG^{8–11,15,16}—the interaction can also be described as stimulated SHG or parametric amplification. Significantly, we showed that the direction of power flow between the two input fields can be changed by varying the relative optical phase.

Here, we take advantage of the phase sensitivity of second-order nonlinear optical interactions by introducing a high-

frequency phase modulation scheme, which produces an intensity modulation in the output beams that can be detected using a standard silicon photodiode and lock-in amplifier. The resulting technique, which we refer to as phase-modulated degenerate parametric amplification (DPA), can retrieve both the magnitude and phase of the second-order nonlinear optical response. The method can be implemented under ambient lighting conditions, is compatible with high-speed laser scanning systems, and provides the enabling option to detect the signal at either the fundamental or second-harmonic frequency. Moreover, the use of 100 fs duration laser pulses renders the technique amenable to spatially resolved ultrafast spectroscopy.^{1,17–19}

We demonstrate the utility of DPA microscopy by imaging multigrain flakes of single-layer MoS₂ grown by chemical vapor deposition (CVD).²⁰ We successfully identify the absolute crystal orientation of each MoS₂ domain and resolve grain boundaries with high signal contrast and sub-diffraction-

Received: May 4, 2018

Revised: June 6, 2018

Published: June 22, 2018

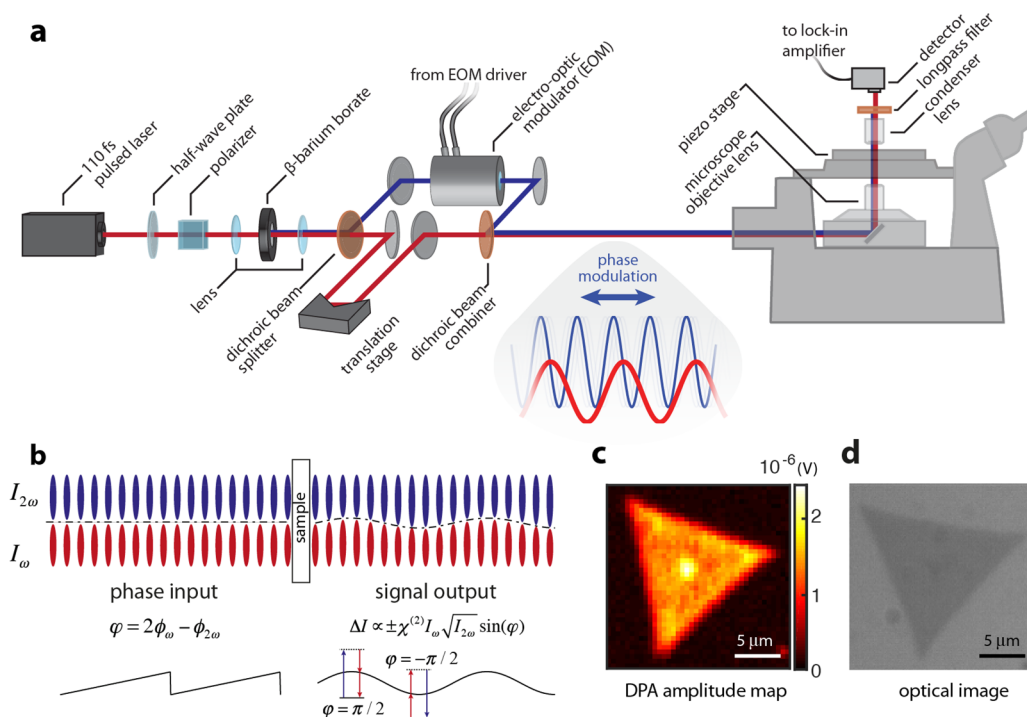


Figure 1. Phase-modulated degenerate parametric amplification (DPA) microscopy. (a) Schematic illustration of the optical apparatus and associated components. In this embodiment, $\lambda = 830$ and 415 nm pulses generated by a Ti:sapphire laser are cross-polarized at the sample, and the fundamental field intensity is measured in transmission using a standard photodiode. (b) Illustration of the working principle of the technique: the electro-optic modulator (EOM) modulates the relative optical phase, φ , between the two laser pulses at 1 MHz according to a sawtooth waveform at 2π modulation depth, generating a sinusoidal variation of the intensity in each field. (c) DPA signal amplitude map of a triangular monolayer MoS_2 flake. (d) Bright-field optical image of the same flake.

limited spatial resolution—information that is usually obtainable only by high-resolution electron microscopy.

Theoretical Foundation. The interaction of a fundamental field with its second harmonic in a nonlinear medium was first described by Armstrong et al. in 1962.²¹ The two fields exchange energy according to the coupled equations

$$\begin{aligned}\frac{du_\omega}{d\zeta} &= u_\omega u_{2\omega} \sin(\varphi) \\ \frac{du_{2\omega}}{d\zeta} &= -u_\omega^2 \sin(\varphi)\end{aligned}\quad (1)$$

where u_ω and $u_{2\omega}$ are the normalized field amplitudes of the fundamental and the second-harmonic fields, ζ is a normalized propagation distance that depends on the second-order nonlinear susceptibility $\chi^{(2)}$, and $\varphi = 2\phi_\omega - \phi_{2\omega}$ is a defined relative optical phase.^{21,22}

When only the fundamental field is incident on the sample, spontaneous SHG occurs. When $u_{2\omega}$ is nonzero, the incident second-harmonic field stimulates either second-harmonic generation (SHG) or difference frequency generation (DFG), depending on the relative optical phase of the fundamental and second-harmonic fields.¹⁴ As a result, the incident fundamental field is either amplified or attenuated by power transfer from (to) the second-harmonic field as the relative optical phase is cycled. This interaction is known as degenerate parametric amplification—a specific case of optical parametric amplification (OPA) wherein the signal and idler frequencies are degenerate.²² As a parametric process, no energy is exchanged with the sample itself, and either beam can be detected to retrieve information about the sample.

The salient difference between DPA and heterodyne-detected SHG is the location of the optical interaction. Classically, heterodyne detection (or second-harmonic interferometry)^{7–10} is described as optical interference at the *detector*, whereas parametric amplification (or stimulated SHG)¹⁴ is described as nonlinear wave mixing within the *sample*. As a result, DPA leads to depletion or amplification of the residual fundamental field, whereas heterodyne SHG does not.²³

Phase-Modulated Degenerate Parametric Amplification Microscopy. The phase-modulated degenerate parametric amplification (DPA) microscopy technique, as illustrated schematically in Figure 1, is performed by rapidly oscillating the relative optical phase between coincident ω and 2ω fields so that power transfer changes direction at MHz frequency. The transmitted (or reflected) laser power of the fundamental ($\lambda = 830$ nm) or second-harmonic ($\lambda = 415$ nm) beam is detected using a standard photodiode, and the magnitude and phase of the DPA signal is retrieved using a lock-in amplifier.

We found that high-frequency phase modulation overcomes difficulties associated with low-frequency phase noise from vibrations, air currents, and other instabilities on the optical table, enabling phase-sensitive measurements to be performed in a laboratory environment that did not have sufficient passive phase stability for heterodyne SHG. Furthermore, careful choice of modulation depth (exactly 2π) and waveform (sawtooth) is essential for making the measurement robust against long-term thermal drift (see Note 1 in the Supporting Information). Phase modulation also overcomes many challenges that are normally associated with high-frequency

intensity modulation, such as fluorescence, transient heating, and differential transmittance/reflectance (i.e., third-order pump–probe signals).

The excellent signal contrast achievable with DPA microscopy is demonstrated on a single-layer MoS₂ flake, shown in Figure 1c,d. For these measurements we used cross-polarized fundamental and second-harmonic laser pulses (~110 fs) generated by a Ti:sapphire laser and detected the residual fundamental field intensity in transmission mode using a silicon photodiode.

Phase-Sensitive Imaging of MoS₂. One of the most critical challenges in characterizing two-dimensional materials is unambiguous determination of the absolute crystal orientation.²⁴ This information is essential for the fabrication of anisotropic 2D heterostructures and devices,²⁵ and for the understanding of 2D materials growth processes.²⁶ In addition, grain boundaries themselves provide opportunities for the discovery of novel physical phenomena.^{27–29} Photoluminescence and Raman are not strongly sensitive to domain rotations, and polarized SHG cannot distinguish between domains with mirror symmetry.^{1,27,30–32} Advanced transmission electron microscopy (TEM) techniques such as high-resolution TEM combined with electron diffraction or scanning-TEM (STEM) can be used to precisely determine crystal orientation and identify grain boundaries, but these techniques are not compatible with optical and electronic substrates,^{33–35} thus preventing *in situ* examination and requiring sample preparations that are delicate and tedious. Here, we show that DPA microscopy is a facile way to retrieve this structural information.

Monolayer MoS₂ has *D*_{3h} symmetry with nonvanishing second-order nonlinear susceptibility tensor components of $\chi_{yyy}^{(2)} = -\chi_{yxx}^{(2)} = -\chi_{xyx}^{(2)} = -\chi_{xyx}^{(2)} = \chi_{xx}^{(2)}$,^{1,36} where the coordinate system is defined with respect to the MoS₂ atomic lattice as shown in Figure S5. For the case of cross-polarized fundamental and second-harmonic fields, the change in fundamental field intensity is given by (see Note 2 in the Supporting Information)

$$\Delta I_{\omega} \propto \chi^{(2)} \cos(3\theta) I_{\omega} \sqrt{I_{2\omega}} \sin(2\phi_{\omega} - \phi_{2\omega}) \quad (2)$$

where θ denotes the orientation of the MoS₂ crystal with respect to the fundamental field polarization, as illustrated in Figure 2, and $\Delta I_{2\omega} = -\Delta I_{\omega}$. Note that both the sign of $\chi^{(2)}$ and the orientation of the MoS₂ crystal determine whether ΔI_{ω} is positive or negative. A 180° rotation of the crystal ($\theta = 0^\circ$ and 180°) will generate an equal amplitude signal, but opposite lock-in phase, as demonstrated in Figure 2.

In lower-symmetry materials, DPA can be used to determine each component of the full nonlinear susceptibility tensor. Each combination of wave vector (with respect to a defined crystal axis), fundamental field polarization, and second-harmonic polarization can be chosen to isolate a specific $\chi^{(2)}$ matrix element.¹⁴ By systematically varying the crystal orientation and input field polarizations, the complete second-order nonlinear susceptibility tensor can be mapped. This approach can be extended to surface and interfacial phenomena in centrosymmetric media, too.

In Figure 3, we characterize a CVD-grown monolayer MoS₂ flake composed of multiple crystal grains with varied orientation. The DPA amplitude and phase maps are shown in Figure 3a,b. The combined amplitude and phase information was used to determine the absolute orientation

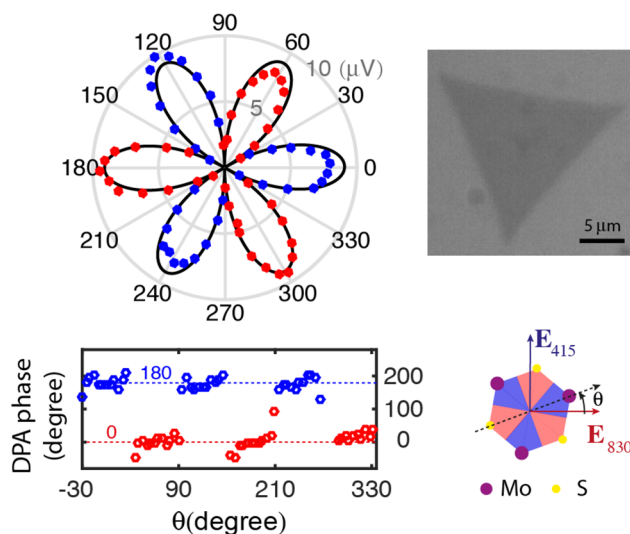


Figure 2. Effect of MoS₂ crystal orientation on DPA amplitude and phase. Rotational dependence of the DPA amplitude (upper panel) and phase (lower panel) for the triangular MoS₂ single-crystal flake shown in the bright-field image. Red and blue colors in two panels indicate a lock-in phase of 0° or 180°, respectively.

of each crystal grain relative to the polarization of the incident fundamental field, as shown in Figure 3c (see Note 3 in the Supporting Information). After identifying the crystal orientation of all grains, the tilt angle between adjacent grains could be determined. The grains I, II, III, and IV are commonly observed neighboring mirror twins with a relative tilt angle of 60°, and their grain boundaries are composed of 4/1 8-member or 4/4 4-member rings.^{33,35} The grains V, VI, and VII have a relative tilt angle of 51°; IV and V have a relative tilt angle of 27°, and I and VII have a relative tilt angle of 33°. These grain boundaries have been predicated by atomistic simulations or observed by other techniques, but the atomic structures have not been identified.^{27,29,30}

DPA Imaging of Grain Boundaries. We demonstrate the capability of resolving grain boundaries with high signal contrast and spatial resolution using DPA microscopy. In Figure 4, we show DPA amplitude and phase maps in the vicinity of a mirror twin boundary in a monolayer MoS₂ flake. The magnitude of the DPA signal scales as $S \propto \chi^{(2)} I_{\omega} \sqrt{I_{2\omega}}$, according to its dependence on the fundamental and second-harmonic field intensities (see Note 1 in the Supporting Information). However, the DPA amplitude goes to zero at the grain boundary due to destructive interference between the second-harmonic fields originating from the left and right sides of the boundary. DPA microscopy has superior signal contrast compared to conventional SHG, which can also be used to resolve the boundary based on a similar mechanism (see Note 5 in the Supporting Information).¹

Line scans of the amplitude (Figure 4c) and phase (Figure 4f) reveal diffraction-limited resolution in the amplitude map (see Note 4 in the Supporting Information) and sub-diffraction-limited resolution in the phase map. The excellent spatial resolution of the phase map is due to the binary nature of this signal; it must be either 180° or 0°, and the spatial resolution is ultimately limited by the vanishing signal intensity at the boundary.

Comparison between DPA and SHG. In Figure 5, we compare DPA imaging to conventional SHG microscopy. In all

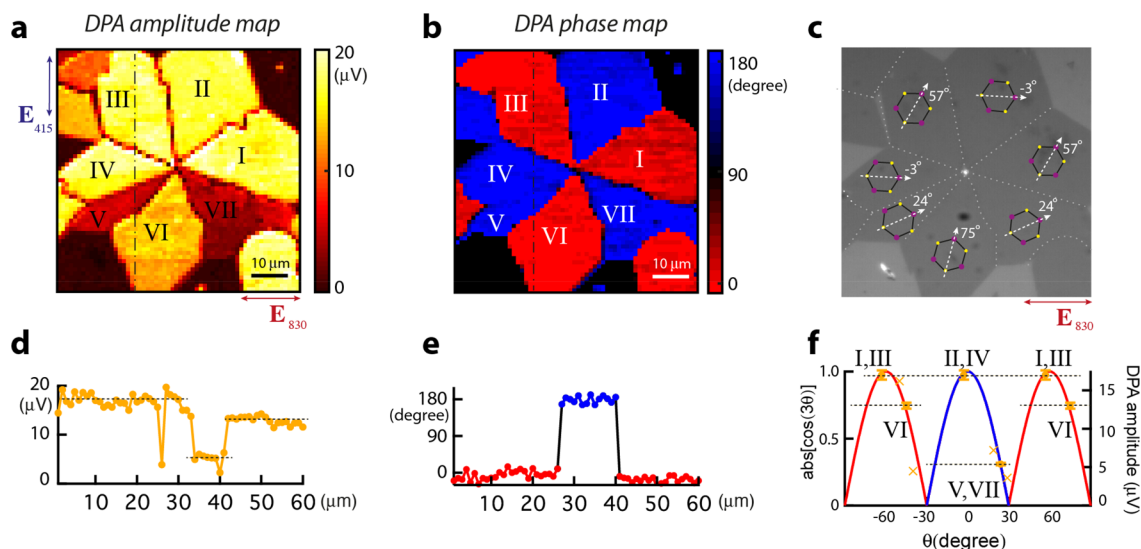


Figure 3. Mapping grain orientations in MoS₂ crystals. (a, b) DPA amplitude and phase maps of a multigrain MoS₂ flake. (c) Bright-field image of the flake mapped in panels a and b, with the boundaries and the absolute orientation of each crystal grain, relative to the polarization of the fundamental field (E_{830}), labeled. (d, e) Line cuts taken along the dash-dotted lines through the images in panels a and b. (f) Universal curve used to determine the crystal orientation of each grain labeled in panel c.

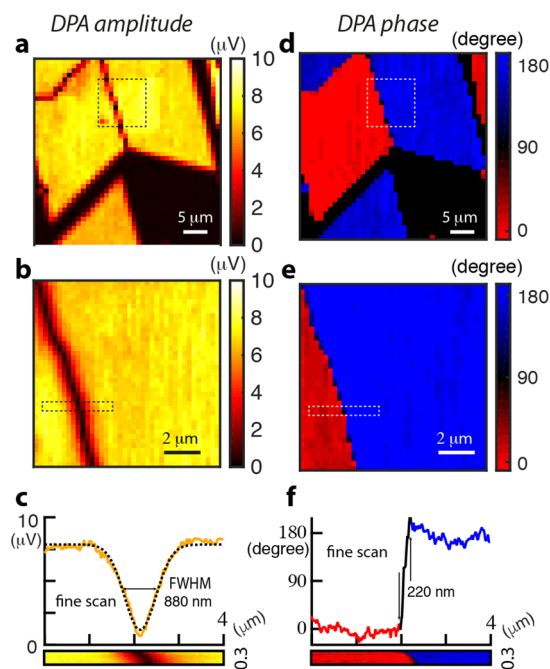


Figure 4. Characterization of grain boundaries. DPA amplitude (a–c) and phase (d–f) mapping near a mirror twin boundary in a monolayer MoS₂ flake.

images, a constant acquisition time of 1 s per pixel was used. The SHG implementation used for comparison is shot-noise-limited, such that the background SHG signal arises only from dark counts of a photomultiplier tube (Hamamatsu R4220P). In contrast, the DPA signal represents a small fluctuation on top of a large background of incident ω or 2ω light that is captured by the photodiode. Because the DPA signal intensity scales with incident 2ω laser power at the same rate as the noise power contained in the incident field, the signal-to-noise ratio for DPA imaging is theoretically equivalent to heterodyne SHG. As with heterodyne SHG, the DPA signal-to-noise ratio

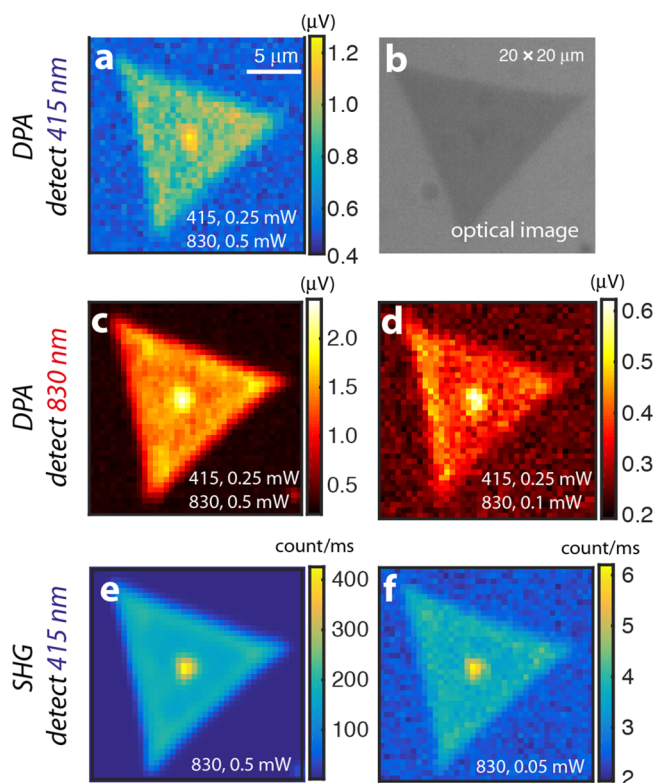


Figure 5. Sensitivity comparison between DPA and conventional SHG. (a) DPA amplitude map acquired with detection at the second-harmonic field wavelength, $\lambda = 415$ nm. (b) Bright-field optical image of the same MoS₂ flake. (c, d) DPA amplitude maps acquired with detection at the fundamental field wavelength, $\lambda = 830$ nm, at two different laser powers. (e, f) Conventional SHG intensity maps acquired using different laser power.

can exceed that of conventional SHG in experiments with high signal background levels.³⁷

DPA offers additional advantages over polarized SHG or heterodyne SHG. First, the signal is contained in both the

fundamental and harmonic fields, so that either beam can be detected as experimental circumstances necessitate. This is particularly useful if the sample, solvent, or substrate is highly scattering or absorptive at the second-harmonic wavelength. Furthermore, the signal intensities are large enough to be detected with a standard silicon photodiode under normal room lighting, and the high-frequency phase modulation scheme enables phase-sensitive measurements to be performed in laboratory environments that do not have sufficient passive phase stability for interferometry. Finally, high-frequency (MHz) phase modulation and lock-in detection is compatible with high-speed laser scanning microscopes. Wide-field signal acquisition could also be achieved (without raster scanning the laser spot) by using microlens arrays with chip-integrated lock-in pixels or tuned amplifier arrays.^{38,39} Beyond 2D materials characterization, we expect DPA to find use in bioimaging, interfacial spectroscopy, and ultrafast microscopy.^{3–5,17,18}

Materials and Methods. Phase-Modulated Degenerate Parametric Amplification (DPA) Microscopy. See Note 6 in the [Supporting Information](#) for detailed optical layout. A Ti:sapphire oscillator (Coherent Mira HP) generated 830 nm laser pulses of ~ 110 fs pulse duration at 76 MHz repetition rate. The $\lambda = 830$ nm laser beam passed through a small aperture (to produce a near-Gaussian beam), a half-wave plate, and a Glan–Taylor polarizer (GT5, Thorlabs), and then was focused into a 0.1 mm thick β -barium borate crystal (BBO, Type 1, Eksma Optics) by a 50 mm focal length lens (~ 8 nJ pulse energy) to generate $\lambda = 415$ nm laser pulses (~ 40 pJ pulse energy). The output beams were recollimated by a 50 mm focal length lens, and then separated by a dichroic beam splitter (042–0845, $>99.5\%$ reflectivity at 800 nm, Eksma Optics). Residual 830 nm light was removed from the 415 nm beam using a colored glass filter (FGS550, Thorlabs). The 415 nm or the 830 nm beam was sent to the EOM, depending on which field was used for detection (see details below and [Figure S11](#)); the detected beam bypassed the EOM. One of the two beams was sent to an optical delay line consisting of mirrors mounted on a linear translation stage (462-X-M, Newport Corporation) driven by a piezoelectric inertia actuator (ZBT225B, Thorlabs). The second harmonic and fundamental paths were recombined by a beam combiner (042-4805 Eksma Optics, $>99.5\%$ reflectivity at 390–410 nm), and were directed into an inverted optical microscope (Nikon Ti–U). The two beams were focused onto the sample by a microscope objective lens (Nikon, CFI S Plan Fluor ELWD, 40 \times , 0.6 numerical aperture), and then directed to an amplified Si photodetector (PDA 36A, Thorlabs) by a 25 mm focus length condenser lens. When the 830 nm (415 nm) laser beam was detected, a long (short) pass filter FGL550S, Thorlabs (FGB 39, Thorlabs), was placed in front of the detector. The signal from the photodetector was fed directly into a lock-in amplifier (HF2LI, Zurich Instruments), and the output was recorded and analyzed by a computer. For spatial mapping, the sample was scanned relative to the stationary focal point using a piezo stage (P-545.xR8S PI nano XY Piezo System, Physikinstrumente). For the sample rotation dependent experiments, a motorized precision rotation stage (PRM1Z8, Thorlabs) was used.

A function generator (4063, BK Precision) generated the sawtooth wave for the EOM driver (Model 275, Conoptics) and supplied the reference signal for the lock-in amplifier. The EOM was a potassium dideuterium phosphate (KD*P) phase modulator (M350-160 phase, Conoptics). To minimize phase

noise, the separated beam paths (dual beam paths from separator to combiner, including the EOM) were placed inside a homemade box to minimize the effects of external disturbances. Inside the box, the EOM was placed on a water-cooled breadboard (Thorlabs) fed by a recirculating chiller (Coherent).

MoS₂ Monolayer Chemical Vapor Deposition (CVD).²⁰ The growth substrate was a 285 nm SiO₂/Si wafer, cleaned by deionized water, acetone, and isopropyl alcohol sequentially before growth. Perylene-3,4,9,10-tetracarboxylic acid tetrapotassium salt (PTAS) molecules were used as the seeding promoter, and two additional clean SiO₂/Si substrates were coated with PTAS as seed reservoirs. The growth substrate was then suspended between those two PTAS seed reservoirs. All of these substrates were faced down and placed on a crucible containing a molybdenum oxide (MoO₃, 99.98%) precursor. This MoO₃ precursor was put in the middle of a 1 in. quartz tube reaction chamber, and another sulfur powder (99.98%) precursor was placed upstream, 14 cm away from MoO₃ precursor, in the quartz tube. Before heating, the CVD system was purged using 1000 sccm of Ar (99.999% purity) for 5 min, and then 20 sccm of Ar was flowed into the system as a carrier gas. Next, the temperature of the reaction chamber was increased to 625 °C at a rate of 30 °C min^{−1}. The monolayer MoS₂ was synthesized at 625 °C for 3 min under atmospheric pressure. The temperature at the position where the sulfur was located was ~ 180 °C during growth. Finally, the system was cooled down to room temperature quickly using an electric fan. During the cooling process, 1000 sccm Ar flow was introduced to remove the reactants, preventing further unintentional reactions.

MoS₂ Transfer Process. The CVD-grown monolayer MoS₂ was transferred onto transparent glass for all the optical measurements by a wet transfer process. First, poly(methyl methacrylate) (950 PMMA A4) was spin-coated (4000 rpm for 1 min) onto the as-grown monolayer MoS₂ samples. Next, the PMMA/MoS₂/SiO₂/Si stack was placed in an aqueous KOH solution, and the solution was then heated up to 85 °C. After the SiO₂ layer was etched away, the PMMA/MoS₂ stack was separated from the substrate and remained floating on the solution. The PMMA/MoS₂ film was then placed in distilled water using a glass slide for 20 min to remove the KOH residue. This rinsing step was repeated three times. After that, the PMMA/MoS₂ film was transferred onto a transparent glass substrate, and was then baked at 80 °C for 10 min and 130 °C for another 10 min. This baking step can remove moisture and enhance the adhesion between MoS₂ and the substrate. Finally, the PMMA/MoS₂/glass stack was immersed in acetone for 12 h to remove the PMMA layer.

■ ASSOCIATED CONTENT

Supporting Information

The Supporting Information is available free of charge on the [ACS Publications website](#) at DOI: [10.1021/acs.nanolett.8b01827](https://doi.org/10.1021/acs.nanolett.8b01827).

Mathematical description of the lock-in signal and its dependence on the optical phase; nonlinear wave mixing in MoS₂; determining the absolute MoS₂ crystal orientation; signal contrast comparison between DPA microscopy and conventional SHG; spatial resolution of the instrument; and optical layout and electronic components ([PDF](#))

AUTHOR INFORMATION

Corresponding Author

*E-mail: tisdale@mit.edu. Phone: +1-617-253-4975. Fax: +1-617-258-5766.

ORCID

Jing Kong: 0000-0003-0551-1208

William A. Tisdale: 0000-0002-6615-5342

Present Address

[†]Y.G.: State Key Laboratory for Mesoscopic Physics and School of Physics, Peking University, Beijing 100871, China.

Author Contributions

Y.G., A.J.G., and W.A.T. conceived of the technique and designed the experiments. Y.G. built the instrument and collected and analyzed the data. P.-C.S. and J.K. supplied the MoS₂ samples and helped interpret results. All authors contributed to the writing of the manuscript.

Notes

The authors declare no competing financial interest.

ACKNOWLEDGMENTS

We thank Richard Kocka at Conoptics Inc. for helpful discussions related to the EOM phase modulator. This work was supported by the U.S. Department of Energy, Office of Basic Energy Sciences, under Award DE-SC0010538. A.J.G. acknowledges partial support from the National Science Foundation under Grant 1122374. P.-C.S. and J.K. acknowledge the support from the Center for Energy Efficient Electronics Science (NSF Award 0939514). Y.G. acknowledges partial support from the Office of China Postdoctoral Council under the international Postdoctoral Exchange Fellowship Program 20140040.

REFERENCES

- (1) Yin, X.; Ye, Z.; Chenet, D. A.; Ye, Y.; O'Brien, K.; Hone, J. C.; Zhang, X. *Science* **2014**, *344* (6183), 488.
- (2) Butet, J.; Brevet, P.-F.; Martin, O. J. F. *ACS Nano* **2015**, *9* (11), 10545–10562.
- (3) Bueno, J. M.; Ávila, F. J.; Artal, P. Second Harmonic Generation Microscopy: A Tool for Quantitative Analysis of Tissues. In *Microscopy and Analysis*; Stanciu, S. G., Ed.; InTech: Rijeka, 2016; Chapter 5.
- (4) Campagnola, P. J.; Dong, C. Y. *Laser Photonics Rev.* **2011**, *5* (1), 13–26.
- (5) Shen, Y. R. *Annu. Rev. Phys. Chem.* **1989**, *40* (1), 327–350.
- (6) Omote, M.; Kitaoka, H.; Kobayashi, E.; Suzuki, O.; Aratake, K.; Sano, H.; Mizutani, G.; Wolf, W.; Podlousky, R. J. *Phys.: Condens. Matter* **2005**, *17* (8), S175.
- (7) Yazdanfar, S.; Laiho, L. H.; So, P. T. C. *Opt. Express* **2004**, *12* (12), 2739–2745.
- (8) Rechsteiner, P.; Hulliger, J.; Flörsheimer, M. *Chem. Mater.* **2000**, *12* (11), 3296–3300.
- (9) Kaneshiro, J.; Uesu, Y.; Fukui, T. *J. Opt. Soc. Am. B* **2010**, *27* (5), 888–894.
- (10) Bancelin, S.; Couture, C.-A.; Légaré, K.; Pinsard, M.; Rivard, M.; Brown, C.; Légaré, F. *Biomed. Opt. Express* **2016**, *7* (2), 399–408.
- (11) Han, Y.; Raghunathan, V.; Feng, R.-r.; Maekawa, H.; Chung, C.-Y.; Feng, Y.; Potma, E. O.; Ge, N.-H. *J. Phys. Chem. B* **2013**, *117* (20), 6149–6156.
- (12) Shaffer, E.; Pavillon, N.; Kühn, J.; Depeursinge, C. *Opt. Lett.* **2009**, *34* (16), 2450–2452.
- (13) Masihzadeh, O.; Schlup, P.; Bartels, R. A. *Opt. Express* **2010**, *18* (10), 9840–9851.
- (14) Goodman, A. J.; Tisdale, W. A. *Phys. Rev. Lett.* **2015**, *114* (18), 183902.

- (15) Rivard, M.; Popov, K.; Couture, C.-A.; Laliberté, M.; Bertrand-Grenier, A.; Martin, F.; Pépin, H.; Pfeffer, C. P.; Brown, C.; Ramunno, L.; et al. *J. Biophotonics* **2014**, *7* (8), 638–646.
- (16) Couture, C.-A.; Bancelin, S.; Van der Kolk, J.; Popov, K.; Rivard, M.; Légaré, K.; Martel, G.; Richard, H.; Brown, C.; Laverty, S.; et al. *Biophys. J.* **2015**, *109* (12), 2501–2510.
- (17) Tisdale, W. A.; Williams, K. J.; Timp, B. A.; Norris, D. J.; Aydil, E. S.; Zhu, X. Y. *Science* **2010**, *328* (5985), 1543.
- (18) Manaka, T.; Lim, E.; Tamura, R.; Iwamoto, M. *Nat. Photonics* **2007**, *1* (10), 581–584.
- (19) Bancelin, S.; Aimé, C.; Gusachenko, I.; Kowalczyk, L.; Latour, G.; Coradin, T.; Schanne-Klein, M.-C. *Nat. Commun.* **2014**, *5*, 4920.
- (20) Ling, X.; Lee, Y.-H.; Lin, Y.; Fang, W.; Yu, L.; Dresselhaus, M. S.; Kong, J. *Nano Lett.* **2014**, *14* (2), 464–472.
- (21) Armstrong, J. A.; Bloembergen, N.; Ducuing, J.; Pershan, P. S. *Phys. Rev.* **1962**, *127* (6), 1918–1939.
- (22) Boyd, R. W. *Nonlinear Opt.*, 3rd ed.; Elsevier: Singapore, 2008.
- (23) Goodman, A. J.; Tisdale, W. A. *Phys. Rev. Lett.* **2016**, *116* (5), 059402.
- (24) Lin, Z.; McCreary, A.; Briggs, N.; Subramanian, S.; Zhang, K.; Sun, Y.; Li, X.; Borys, N. J.; Yuan, H.; Fullerton-Shirey, S. K.; et al. *2D Mater.* **2016**, *3* (4), 042001.
- (25) Das, S.; Robinson, J. A.; Dubey, M.; Terrones, H.; Terrones, M. *Annu. Rev. Mater. Res.* **2015**, *45* (1), 1–27.
- (26) Najmaei, S.; Yuan, J.; Zhang, J.; Ajayan, P.; Lou, J. *Acc. Chem. Res.* **2015**, *48* (1), 31–40.
- (27) Zhang, Y.; Zhang, Y.; Ji, Q.; Ju, J.; Yuan, H.; Shi, J.; Gao, T.; Ma, D.; Liu, M.; Chen, Y.; et al. *ACS Nano* **2013**, *7* (10), 8963–8971.
- (28) Pulkkinen, A.; Yazyev, O. V. *Phys. Rev. B: Condens. Matter Mater. Phys.* **2016**, *93* (4), 041419.
- (29) Gao, N.; Guo, Y.; Zhou, S.; Bai, Y.; Zhao, J. *J. Phys. Chem. C* **2017**, *121* (22), 12261–12269.
- (30) Park, S.; Kim, M. S.; Kim, H.; Lee, J.; Han, G. H.; Jung, J.; Kim, J. *ACS Nano* **2015**, *9* (11), 11042–11048.
- (31) Karvonen, L.; Säynätjoki, A.; Huttunen, M. J.; Autere, A.; Amirsolaimani, B.; Li, S.; Norwood, R. A.; Peyghambarian, N.; Lipsanen, H.; Eda, G.; et al. *Nat. Commun.* **2017**, *8*, 15714.
- (32) Ji, Q.; Kan, M.; Zhang, Y.; Guo, Y.; Ma, D.; Shi, J.; Sun, Q.; Chen, Q.; Zhang, Y.; Liu, Z. *Nano Lett.* **2015**, *15* (1), 198–205.
- (33) van der Zande, A. M.; Huang, P. Y.; Chenet, D. A.; Berkelbach, T. C.; You, Y.; Lee, G.-H.; Heinz, T. F.; Reichman, D. R.; Muller, D. A.; Hone, J. C. *Nat. Mater.* **2013**, *12* (6), 554–561.
- (34) Najmaei, S.; Liu, Z.; Zhou, W.; Zou, X.; Shi, G.; Lei, S.; Yakobson, B. I.; Idrobo, J.-C.; Ajayan, P. M.; Lou, J. *Nat. Mater.* **2013**, *12* (8), 754–759.
- (35) Zhou, W.; Zou, X.; Najmaei, S.; Liu, Z.; Shi, Y.; Kong, J.; Lou, J.; Ajayan, P. M.; Yakobson, B. I.; Idrobo, J.-C. *Nano Lett.* **2013**, *13* (6), 2615–2622.
- (36) Kumar, N.; Najmaei, S.; Cui, Q.; Ceballos, F.; Ajayan, P. M.; Lou, J.; Zhao, H. *Phys. Rev. B: Condens. Matter Mater. Phys.* **2013**, *87* (16), 161403.
- (37) Thiansathaporn, P.; Superfine, R. *Opt. Lett.* **1995**, *20* (6), 545–547.
- (38) Liao, C.-S.; Slipchenko, M. N.; Wang, P.; Li, J.; Lee, S.-Y.; Oglesbee, R. A.; Cheng, J.-X. *Light: Sci. Appl.* **2015**, *4*, e265.
- (39) Lioe, D.; Mars, K.; Kawahito, S.; Yasutomi, K.; Kagawa, K.; Yamada, T.; Hashimoto, M. *Sensors* **2016**, *16* (4), 532.